ORIGINAL ARTICLE

Modeling of complex interfaces: Gadolinium-doped ceria in contact with yttria-stabilized zirconia

Xavier Aparicio-Anglès[1] (iD) | Nora H. de Leeuw[1,2]

[1]Department of Chemistry, University College London, London, UK

[2]School of Chemistry, Cardiff University, Cardiff, UK

Correspondence
Xavier Aparicio-Anglès, Department of Chemistry, University College London, London, UK.
Email: x.aparicio-angles@ucl.ac.uk

Funding information
Engineering and Physical Sciences Research Council, Grant/Award Number: EP/K001329/1, EP/K016288/1, EP/L000202.

Abstract

Gadolinium-doped ceria (GDC) and yttria-stabilized zirconia (YSZ) are well-known electrolyte materials in solid oxide fuel cells (SOFCs). Although they can be used independently, it is common to find them in combination in SOFCs, where they are used as protective layers against the formation of secondary phases or electron conduction blockers. Despite their different optimum operating temperatures, it appears that oxygen conduction is not affected by their interface. However, the intrinsic mechanisms of oxygen diffusion at these interfaces still remain unclear. One of the main difficulties when modeling the contact between different materials, or indeed different particles of the same material, is caused by the structural complexity of these systems. If we wish to evaluate the properties of the materials, we first need to obtain a model that includes the main features of the GDC/YSZ interface, such as large-scale defects or cation interdiffusion in the contiguous phase. Since the generation of such a mixed system is complicated, we show here how the "amorphization and recrystallization" strategy can help us to obtain realistic systems. In this, the first of our papers on the structure and properties of layered GDC/YSZ materials, we discuss the structural features of the grain boundary between GDC and YSZ obtained by molecular dynamics simulations.

KEYWORDS

cerium/cerium compounds, dislocations, dopants/doping, grain boundaries, yttria-stabilized zirconia

1 | INTRODUCTION

Solid oxide fuel cells (SOFC) are of significant interest to the scientific community due to their high energy conversion efficiency and fuel flexibility, in combination with a very low environmental impact.[1] SOFCs comprise three main parts: the anode, which normally consists of metal nanoparticles supported on a metal oxide that also acts as the electrolyte; the electrolyte itself; and the cathode, which is normally a perovskite material.

At the anode, CO and H_2 react with the O^{2-} that is generated at the cathode from the reduction of O_2 and transported through the electrolyte, producing CO_2 and H_2O. Normally, anodic reactions take place at the triple phase boundary (TPB), which is where the reaction mixture, the metal nanoparticles, and the electrolyte meet.[2] Thus, after the reaction takes place, the oxygen can be automatically driven toward the cathode. Gadolinium-doped ceria (GDC) and yttria-stabilized zirconia (YSZ) are two well-known doped metal oxides used for that purpose.[3-5] Although isostructural, they exhibit different properties, and one of the more important differences is in their working temperatures. The required temperature for optimal ionic conduction in YSZ is between 873 and 1273 K, whereas in GDC this temperature is lower, that is, between 775 and 1075 K.[6,7]

This variance in optimum working temperature can be explained in terms of the different contributions to the activation energy of the oxygen diffusion process, which are the association and the migration energy. The former relates to the energetic stabilization of oxygen vacancies in the materials due to their Coulombic interaction with the gadolinium and yttrium dopants in GDC and YSZ, respectively, whereas the latter describes the energy required to move one oxygen to a neighboring vacancy. Association energies for $[Gd'_{Ce} - V^{\cdot\cdot}_O - Gd'_{Ce}]$ are slightly lower than for $[Y'_{Zr} - V^{\cdot\cdot}_O - Y'_{Zr}]$, that is, around 0.10 and 0.20 eV for GDC, but between 0.3 and 0.35 eV for YSZ. However, the differences between the migration energies are larger, with GDC showing values between 0.70 and 0.80 eV while YSZ has migration energies between 0.90 and 1.25 eV, thus showing that global activation energies for GDC are easier to overcome than for YSZ.[8,9]

Unfortunately, despite their extensive usage, both materials present some drawbacks. YSZ has been shown to react with the cathode material, which is normally $La_{(1-x)}Sr_xMnO_{(3-x/2)}$ (LSMO) or similar perovskites. As a consequence, highly resistive phases of $SrZrO_3$ or $La_2Zr_2O_7$ are formed, reducing the performance of the cell.[10,11] One way to prevent their formation is to use a protective layer between the materials, which is normally GDC.[12-14] Hence, it would seem logical to use GDC instead of YSZ, but unfortunately above 600°C and under low oxygen partial pressure, Ce^{4+} is reduced to Ce^{3+}, thus inducing electronic conductivity. The electronic conductivity can be blocked while maintaining the ionic conductivity through the introduction of a thin layer of YSZ in the GDC matrix,[15] this GDC/YSZ bilayered electrolyte also presents some inconveniences. During sintering, GDC and YSZ can react, potentially leading to the formation of an interdiffusion layer, which can also decrease the performance of the fuel cell.[16,17]

Although mixtures of the two materials are used as electrolytes, little is known about the interface between GDC and YSZ. Even though in-depth understanding of the reactivity and its structural consequences on the materials, as well as the diffusion behavior of the oxygen anions, may suggest improvements to the materials' performance. There are several techniques that can be used to model the interface, but the easiest and most practical one is by molecular dynamics simulations, which has been shown to produce accurate and reliable results for related materials.[18-20] Here, we therefore introduce a strategy that is capable of modeling, in a realistic fashion, the interface between GDC and YSZ, using interatomic potentials and molecular dynamics simulations.

2 | COMPUTATIONAL DETAILS

The generation of a realistic model for the interface between gadolinium-doped ceria (GDC) and yttria-

stabilized zirconia (YSZ) was achieved using a combination of the METADISE code[21,22] and the DL_POLYv4 code.[23-25] Both codes used the same types of interatomic potentials to describe the interaction between the different atomic species, with the main difference that the META-DISE is used only for static calculations, whereas DL_POLY is used for the molecular dynamics simulations. A brief description of the theoretical background to METADISE, and how it treats surfaces and interfaces can be found in the electronic supporting information (ESI) and Figure S1.

Since both materials are ionic solids, we have assumed the Born model in which the interaction between ions is described by attractive long-range Coulombic terms, balanced by short-range repulsive interactions and van der Waals forces. These latter interactions are evaluated in both codes using the Buckingham potential, expressed as in Equation 1:

$$U_{ij} = A_{ij} \times e^{\left(-\frac{r_{ij}}{\rho_{ij}}\right)} - \frac{C_{ij}}{r_{ij}^6} \qquad (1)$$

where A_{ij} (eV), ρ_{ij} (Å), and C_{ij} (eV·Å^6) are parameters between atoms i and j that are used to fit the equation to experimental data. The Buckingham potentials used throughout this work are listed in Table 1,[26-28] and they all have proved to reproduce lattice parameters, volume expansion, or defect association energies for the corresponding materials GDC and YSZ.[29-33]

The electrostatic interactions are evaluated in both programs using the Ewald summation, which calculates this interaction in both the real and the reciprocal space, also including a self-interaction correction term. It is worth noting that DL_POLY4 uses the smoothed particle mesh Ewald (SPME) method,[34] which, however, only differs from the standard Ewald summation in the treatment of the reciprocal space terms. Finally, two different ensembles were used in the molecular dynamics simulations: the microcanonical ensemble (NVE) and the Hoover isobaric ensemble (NPT).[35]

TABLE 1 Buckingham potential parameters for the different anion-anion and anion-cation interactions. Cation-cation interactions are assumed to be 0

	A (eV)	ρ (Å)	C (eV·Å^6)
O^{2-}-O^{2-}	22764.30	0.1490	27.89
Ce^{4+}-O^{2-}	1986.83	0.3510	20.40
Gd^{3+}-O^{2-}	1336.80	0.3551	0.00
Y^{3+}-O^{2-}	1345.10	0.3491	0.00
Zr^{4+}-O^{2-}	985.87	0.3760	0.00

3 | CONSTRUCTION OF THE MODEL

One of the concerns when modeling grain boundaries (GBs) between different materials is the lattice misfit (F), which is originated when the materials that are in contact have different lattice parameters. The experimental lattice parameters of CeO_2 and cubic ZrO_2 (c-ZrO_2) are 5.411 Å and 5.095 Å, respectively,[36-38] although doping may increase them.[39,40] With our interatomic potentials, the calculated lattice parameters for ceria and zirconia are 5.429 Å and 5.076 Å, respectively, which are in perfect agreement with the experimental values.

The F between these two materials can thus be calculated as:

$$F = \frac{n \cdot a_{CeO_2} - m \cdot a_{c-ZrO_2}}{(n \cdot a_{CeO_2} + m \cdot a_{c-ZrO_2})/2} \quad (2)$$

where a_{CeO_2} and a_{c-ZrO_2} are the lattice parameters of each material, and n and m are the number of repetitions of each unit cell, respectively. In Equation 2, n relates to CeO_2 and m relates to c-ZrO_2. Hence, using the aforementioned bulk parameters and Equation 2, F between CeO_2 and c-ZrO_2 is 6.01%. According to the experimental lattice parameters for YSZ and GDC, which are 5.423 Å and 5.140 Å, respectively,[39,40] the lattice misfit that we would expect for them is 5.36%, and it has been reported to be around 6.00% for the GDC and YSZ bulk materials, depending on the dopant concentration. From experimental data, we know that this lattice misfit, at least in the case of CeO_2/YSZ, is accommodated through dislocations in both materials,[41,42] so we would expect similar structural defects for the GDC/YSZ interface.

Another factor to bear in mind is cation diffusion. Harris et al.[43] indicated that, when considering heteroepitaxial systems, cation exchange at the interface is likely to occur, generating a so-called interdiffusion layer. In view of these structural complexities, the construction "by hand" of a realistic model becomes impossible.

The most plausible strategy to obtain a model that includes all the aforementioned defects is the amorphization and recrystallization (A&R) strategy, which has been pioneered and used by Sayle and coworkers in a number of different systems, including SrO/MgO[20] and CeO_2/YSZ.[31,33] This strategy can be divided into two different steps. First, we generate an ideal structure that minimizes the lattice misfit between GDC and YSZ, by finding a specific near coincidence site lattice (NSCL).[33] Next, we search for a lower energy configuration, using the previous system as a starting point, by increasing the ionic mobility, that is, by bringing the system to a temperature close to the melting point. In time, we recrystallize the system by applying a high pressure while maintaining a high temperature. Finally, once the system is recrystallized, we release the pressure and gradually cool it down until we reach a temperature close to 0 K.

3.1 | Near coincidence site lattice

The near coincidence site lattice (NCSL) consists of finding particular supercells for both GDC and YSZ, which minimize the lattice misfit between the two materials as much as possible. Normally, the lattice parameters that are used are those belonging to the respective bulks. However, since the (111) surface is the facet that is the contact between GDC and YSZ,[44,45] we decided to use their surface lattice parameters instead. Accordingly, it seems logic to use the experimental lattice parameters for GDC and YSZ to find the corresponding NCSL. However, we decided to use the calculated lattice parameters for CeO_2 and ZrO_2 instead, mainly because of two reasons. First, any model is usually based on the calculated lattice parameters and not on the experimental ones. Consequently, we should calculate the GDC and YSZ parameters, but that would involve calculating a large amount of unit cells with different dopant concentrations and distributions. Second, if we were using the doped bulks, the surfaces and grain boundaries that we would obtain would suffer a great reconstruction, because of the impossibility of finding nonpolar terminations.

We thus started by generating a slab model for the (111) surface of both parent materials (CeO_2 and c-ZrO_2) using the METADISE code. The (111) surface for a fluorite-type system has two different nonpolar terminations: metal (M_t) and oxygen (O_t), respectively, as shown in Figure 1B,C, respectively. The relaxed surface energy (γ_r) obtained for these terminations was 3.90 and 1.58 J·m^{-2}, respectively, indicating that the O_t is the most stable termination, as expected from the fact that it is a nonreconstructed stoichiometric Tasker type II surface,[22] whereas M_t is a reconstructed dipolar type III surface, which are generally unstable surfaces.

Next, the two surfaces were used to generate the grain boundaries (GBs). There are two main types of GBs: tilt and twist. Tilt GBs are obtained when the rotation axis of one grain is parallel to the GB's plane, whereas twist GBs are obtained when this rotation axis is perpendicular to the GB's plane (see Figure S2 in the ESI). In this work we only considered tilt GBs generated by reflection of the slab model. Since γ_r relates to the stability of the surface but not to the GB, we studied the GBs originated by reflection of both M_t and O_t terminations and calculated the relative stabilities of the two GB systems. As c-ZrO_2 is not stable under standard conditions,[46] we performed this step only for CeO_2, assuming that the results we obtained would be transferable to c-ZrO_2.
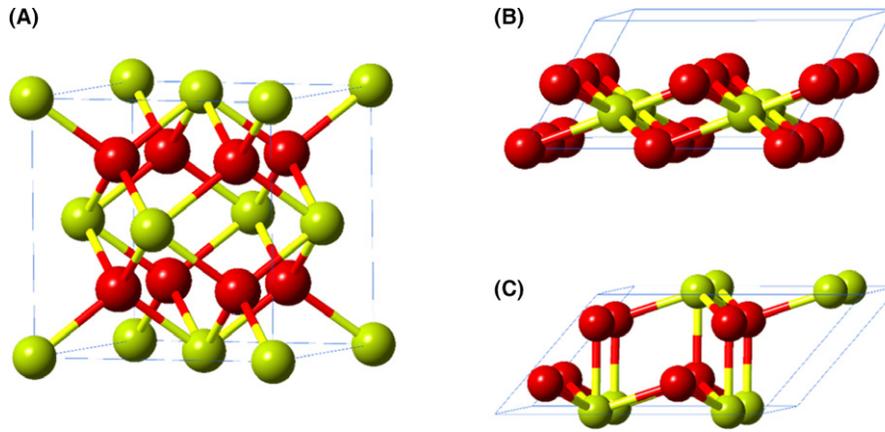
(A)

(B)

(C)

FIGURE 1 Ball and stick representation of (A) fluorite-type unit cell; (B) oxygen termination of the (111) surface derived from a fluorite-like system; and (C) metal termination of the (111) surface derived from a fluorite-like system. Cations are represented in green, whereas oxygen atoms are represented in red. Atomic radii are chosen randomly to aid clarity [Color figure can be viewed at wileyonlinelibrary.com]

After slab reflection, we calculated the interface potential energy surface (IPES) by scanning the relative position of one grain with respect to the other. This procedure allowed us to identify the grain arrangement that lowered the energy for both terminations, as shown in Figure 2. For simplicity, from now on we will label these grain boundaries GB-O_t and GB-M_t, respectively.

For the lowest energy GB arrangement, we calculated the formation energy (E_f) and the cleavage energy (E_c), according to Equations 3 and 4:

$$E_f = E_{GB} - E_B \quad (3)$$

$$E_c = 2E_S - E_{GB} \quad (4)$$

where E_{GB} is the total energy of the grain boundary, E_B is the bulk energy, and E_S is the energy of the surfaces. According to Equations 3 and 4, E_f is the formation energy with respect to the bulk materials and E_c accounts for the energy required to separate two grains thereby exposing their surfaces. Therefore, the most favorable GB will be the one that minimizes E_f but maximizes E_c.

E_f for both GBs is calculated to be approximately the same: 1.87 J·m^{-2} for GB-O_t and 1.94 J·m^{-2} for GB-M_t, respectively. Interestingly, E_c for GB-O_t is 1.29 J·m^{-2}, but for GB-M_t is 6.26 J·m^{-2}, that is, despite having approximately the same formation energy, GB-M_t is more stable than GB-O_t, conversely to what we observed with the clean surfaces. Consequently, we have continued our study focusing only on the M_t grain boundary.

In the M_t slab, we next substituted certain Ce and Zr for Gd and Y and generated the corresponding oxygen vacancies in order to keep the electroneutrality of the system. The dopant concentration is derived from the general stoichiometric expression of GDC, which is $Ce_{(1-x)}Gd_xO_{(2-x/2)}$, which also applies for YSZ as $Zr_{(1-x)}Y_xO_{(2-x/2)}$. Hence, our model simulates a dopant concentration of x=0.14, that is, 14% for both GDC and YSZ. Although this concentration is somewhat higher than the usual experimental one, which are 8% for YSZ and 20% for GDC, it is still found within the range of the acceptable concentrations.[11,16,47-49] In addition, we transformed the hexagonal (111) surface unit cell into a rectangular (111) surface unit cell for computational simplicity. Therefore, we had to locate the NSCL for $\vec{b}$ and $\vec{c}$ vectors, respectively, which are both lateral to the surfaces.

Thus, according to Equation 2, n and m are equal to 1, F was 6.78% in both directions, which was minimized to 0.18% for orthorhombic b direction and to 0.17% for the orthorhombic c direction, respectively, by considering n=14 and m=15 in both directions (see Table 2). Hence, the dimensions of the simulation box that will contain both thin layers will be $\vec{b} \approx$ 107.70 Å and $\vec{c} \approx$ 186.50 Å. Finally, normal to the surface $\vec{a}$ 50.00 Å, resulting from the height of the GDC slab of 22.959 Å, the YSZ slab of 20.539 Å, and an initial distance between the materials, which we set at 3 Å per side. If we had assumed the experimental lattice parameters for GDC and YSZ instead, which are listed in Table 2 as well, the lattice misfit would have also been minimized by considering n=14 and m=15, but with a slightly larger F of 1.54%. This difference between lattice misfits is indicative that it is likely that we are potentially introducing strain in our system. If that were the case, we would expect the presence of large-scale defects once the A&R is finished.

3.2 | Amorphization and recrystallization

For the A&R, we have used two different ensembles: NVE and NPT. As it has been shown that with constant pressure ensembles, the system retains its original structure,[33] NVE was used for the amorphization step, which consisted of melting both materials for a very short period of time
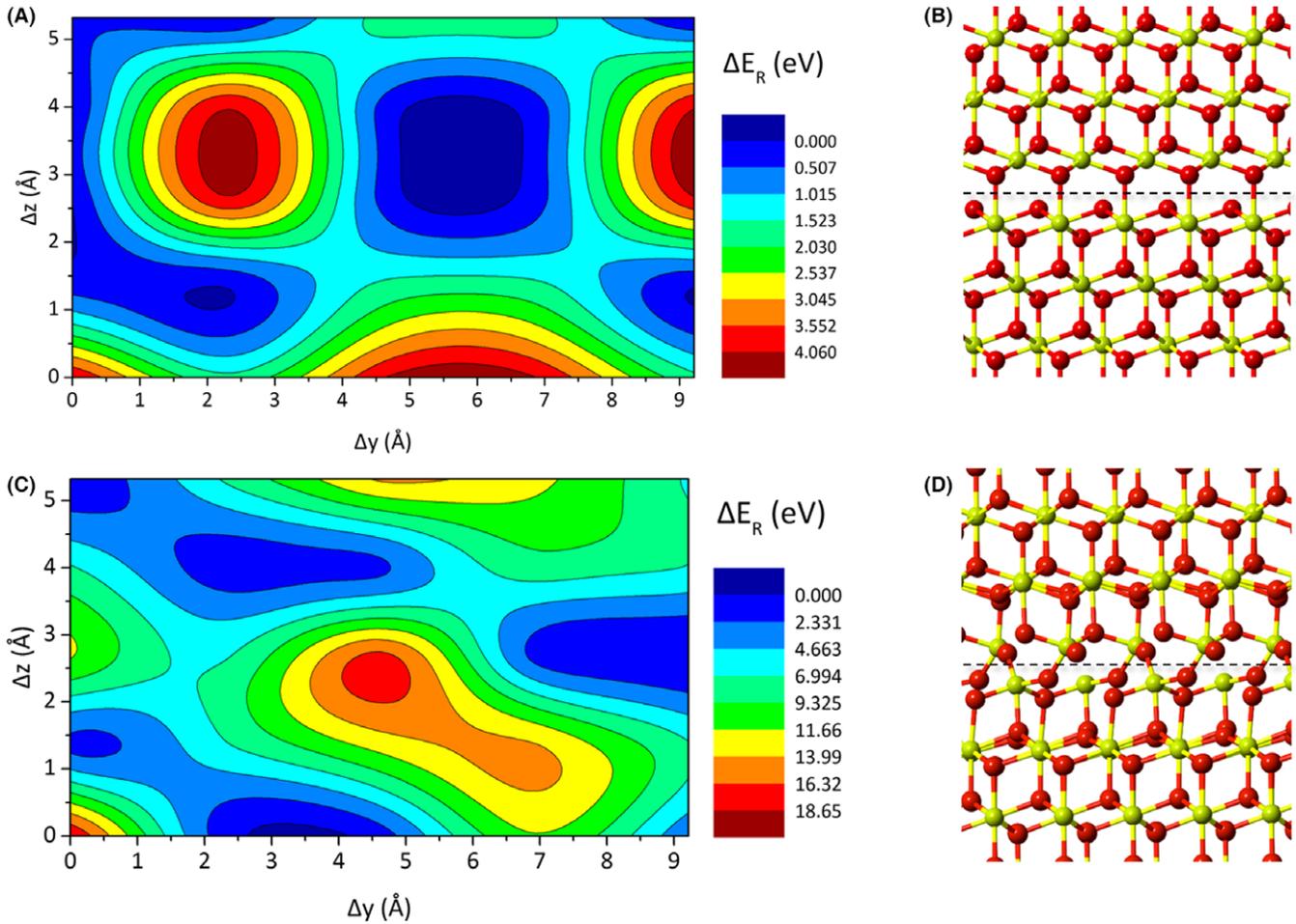
FIGURE 2   IPES for (A) GB-O$_t$ and (C) GB-M$_t$, and the corresponding ball and stick representations for (B) GB-O$_t$ and (D) GB-M$_t$ which is lower in energy [Color figure can be viewed at wileyonlinelibrary.com]

TABLE 2   Lattice parameters for the bulk, (111) hexagonal (hex), and orthorhombic (ort) unit cells for calculated CeO$_2$ and ZrO$_2$, and experimental GDC and YSZ

	bulk	hex	ort b	ort c	ort supercell b	ort supercell c
CeO$_2$	5.429	7.677	7.677	13.297	107.480	186.162
ZrO$_2$	5.076	7.178	7.178	12.432	107.668	186.486
GDC	5.423	7.669	7.669	13.282	107.359	185.952
YSZ	5.140	7.269	7.269	12.589	109.028	188.831

Note that the surface lattices refer to the formal 2 × 2 (111) unit cell. All lattice parameters are in Å.

(30 ps), as listed in Table 3. After randomization, we applied 200 katm using an NPT ensemble for to recrystallize the system, which also involved a compression of the cell. The selection of this pressure is independent of any experimental pressure and its only purpose is to speed up the crystallization phase.[33] After 3.3 ns, the system was fully crystallized and we proceeded first to release the pressure, with a production run of 3 ns, followed by a controlled cooling down of the system to 10 K.

TABLE 3   Detailed list of the ensembles, temperatures, pressures, and production runs used for the different steps of the A&R strategy

Step	Ensemble	T (K)	P (katm)	t (ps)
Amorphization	NVE	3400	0	30
Recrystallization	NPT	3400	200	3300
	NPT	3400	0	3000
Cooling down	NPT	3000	0	2000
		2500	0	2000
		2000	0	1000
		1500	0	1000
		1000	0	1000
		500	0	1000
		0 (10)	0	1000

4 | RESULTS AND DISCUSSION

4.1 | Structural analysis

After applying the A&R process, the dimensions of the system have changed significantly. The height of the unit

cell ($\vec{a}$ direction) has increased by 14.73 Å, from 50.00 Å to 64.73 Å, which represents an increment of 29.45%. Consequently, the length and width ($\vec{b}$ and $\vec{c}$ directions, respectively) have decreased by 17.2% and 17.7%, respectively (from 107.70 Å to 89.01 Å for $\vec{b}$, and from 186.50 Å to 157.75 Å for $\vec{c}$).

From a visual analysis of Figure 3, the bulk does not show any void regions, and full crystallinity seems to be recovered. However, the layer structure is clearly not as regular as it was prior to A&R. In the initial geometry (Figure 3A), both GDC and YSZ had seven metal atomic layers, but after A&R (Figure 3B) each material has now between 10 and 12 metal layers, depending on the region. This is a clear indication that the bulk is now less regular than it was before, so the presence of large-scale defects, such as dislocations, is expected.

For a more detailed analysis, we have divided the system into different sections in order to identify the presence of any defects. As a representative sample, we will discuss two different slices, shown in Figure 4. Figure 4A illustrates a section of the material where full crystallinity is almost recovered. However, some local disorder can be observed at the interface between GDC and YSZ, as well as a degree of cation diffusion that has taken place between the two phases. It is also worth noting that the upper GDC phase is slightly bent, which is an expected distortion when there is a small lattice misfit between materials,[41] although no clear dislocations are observed.

In contrast, the section depicted in Figure 4B shows a different scenario. Here, despite the fact that a crystalline arrangement can also be identified, the upper interface is clearly irregular, which agrees with experimental evidence for a roughness between materials.[31] Moreover, we observe a less dense region in the left-hand side of the YSZ phase

along the $\vec{a}$ direction. Conversely, the GDC shows a major densification in the same region. A closer look reveals that this higher densification is actually a series of successive screw dislocations that are depicted in more detail in Figure 4C. This series of dislocations, primarily located in the upper GDC phase, lead to what appears to be the start of a crack in the lower GDC phase, which is being filled by YSZ, and could explain why the YSZ is less dense in the upper grain boundary. The presence of the dislocations and the slight bending of the GDC phase give rise to apparent different domains, highlighted in blue on the left in Figure 5. It thus seems quite clear that despite the low lattice misfit achieved by using the NSCL based on the CeO_2 and ZrO_2 lattice parameters, this apparent epitaxy was lost during the A&R, and is now accommodated through a series of defects. Also, based on the different distribution of defects across our model, it seems clear that the strain is not uniform within our material, as it happens in any real system.

The presence of these large-scale defects in our model somehow differs from a similar interface obtained using the A&R methodology. Sayle et al. use the A&R to obtain a realistic grain boundary for CeO_2 and YSZ.[33] Unlike us, during the recrystallization phase they were able to dissolve the different grains that were formed during the process. Although we have used the exact same strategy, the main difference between their model and ours is that they base the construction of the NCSL on the experimental lattice parameters of CeO_2 and YSZ.

That unequivocally brings us back to whether our assumption of considering the lattice parameters of the calculated parent materials (CeO_2 and ZrO_2) was right or not. As we were expecting, the small strain originated from the remaining s lattice misfit in our NCSL is the responsible of the different large-scale defects that we obtain. Therefore, that implies that unless we are considering the experimental (or calculated) lattice parameters for the doped systems, we will have large-scale defects in our model. However, experimental interfaces do show large-scale defects, which are included in our model. Hence, we conclude that despite not fully minimizing the lattice misfit with our approximation, the overall result is improved by their presence making our system to be more realistic.

4.2 | Dopant distribution and clustering

The cation diffusion shown in Figure 4 is corroborated by the atomic percentage profile, illustrated on the right in Figure 5. This profile clearly shows cation penetration between GDC and YSZ, and also reveals that this effect is larger for Ce^{4+} and Zr^{4+} than for the dopants Gd^{3+} and Y^{3+}. According to the concentration profile, Ce^{4+} and Zr^{4+} penetrate about 7 Å inside the contiguous phase, and so does Y^{3+}, which is the same behavior as observed
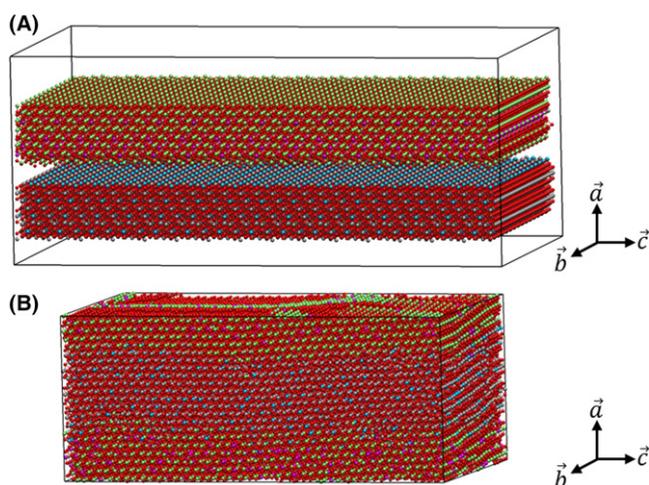

FIGURE 3 Ball and stick representation of the GDC/YSZ system (A) before and (B) after applying A&R [Color figure can be viewed at wileyonlinelibrary.com]
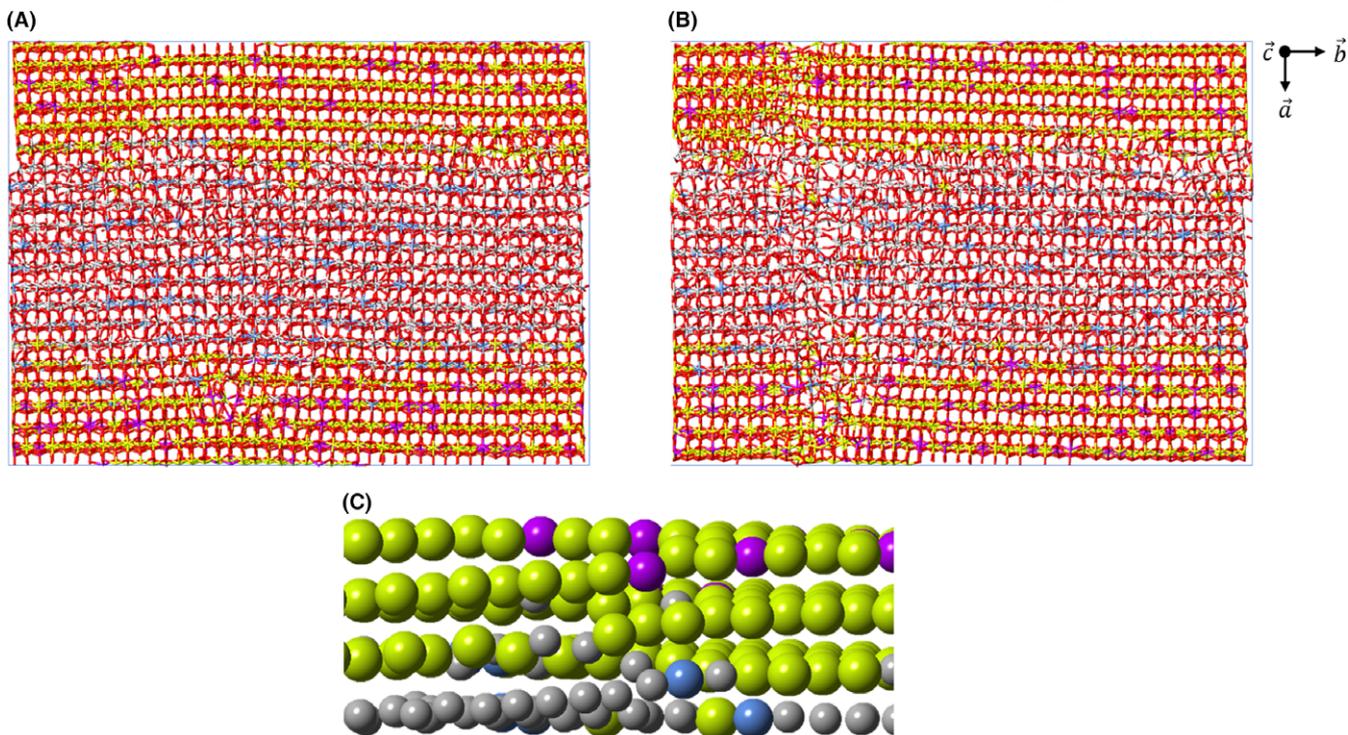
FIGURE 4 A and B, Stick representations of two different sections of the GDC/YSZ bulk. C, ball representation of a screw dislocation observed in the GDC phase near the interface with YSZ, with the oxygen atoms omitted for clarity. Ce^{4+}: green, Gd^{3+}: magenta, O^{2-}: red, Y^{3+}: blue, and Zr^{4+}: gray. [Color figure can be viewed at wileyonlinelibrary.com]
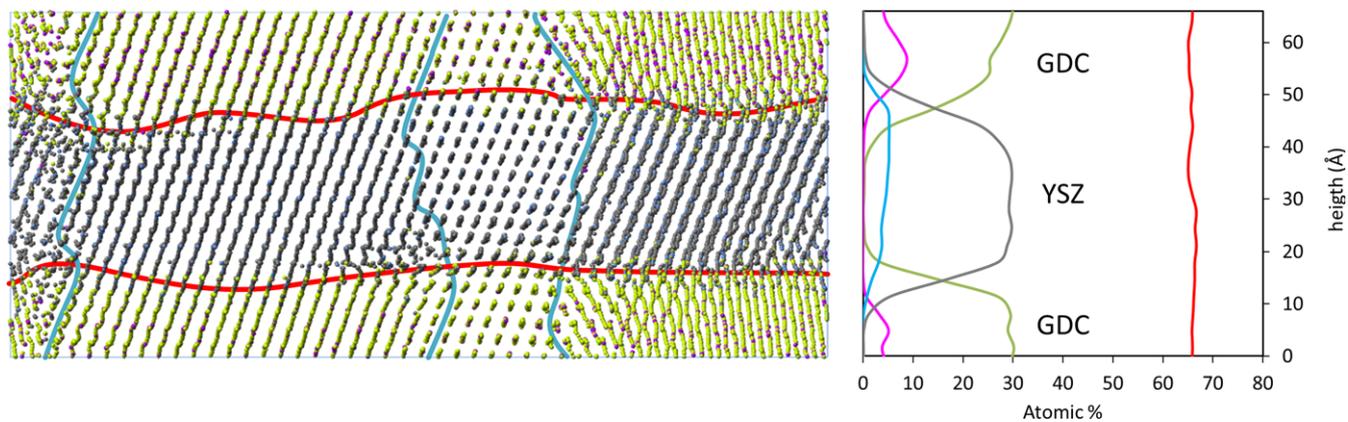

FIGURE 5 (Left) Ball and stick representation of the GDC/YSZ model obtained after applying A&R strategy. Oxygen atoms are not represented for simplification. (Right) Concentration profile for the different atomic species. Ce^{4+}: green, Gd^{3+}: magenta, O^{2-}: red, Y^{3+}: blue, and Zr^{4+}: gray [Color figure can be viewed at wileyonlinelibrary.com]

experimentally by Knibbe et al.[50] In contrast, Gd^{3+} barely penetrates inside YSZ phase, which is probably a consequence of its initial distribution in the CeO_2 matrix. One could argue that the gadoliniums' atomic mass is related to its lower mobility during the amorphization phase and thus explain why Gd^{3+} shows less penetration. However, if true, we would expect a correlation between penetration and atomic mass, and this is not the case.

Cation penetration in the contiguous phase is an expected phenomenon, as the formation of $Ce_\alpha Gd_\beta Y_\gamma Zr_\varepsilon O_{2-\zeta}$

mixtures is very common, and among other applications, is exploited to prevent delamination between GDC/YSZ.[16,51,52] In this case, however, no interdiffusion layer is formed, since the time spent to randomize the system during A&R was deliberately kept short in order to avoid this behavior. Nonetheless, it is worth mentioning that the cation interdiffusion is mainly controlled by the length of the amorphization phase. Therefore, if we were intending to study the formation and behavior of the interdiffusion layer, we would only need to run a longer randomization

simulation. Finally, in the concentration profile, we also included the oxygen concentration, which remains constant throughout the different materials.

Aside from the cation penetration, we also assessed whether dopants are uniformly distributed throughout the bulk, which is important in order to evaluate the possible formation of different phases that could develop due to dopant clustering or the formation of an interdiffusion layer. We therefore analyzed the radial distribution function (RDF), as shown in Figure 6.
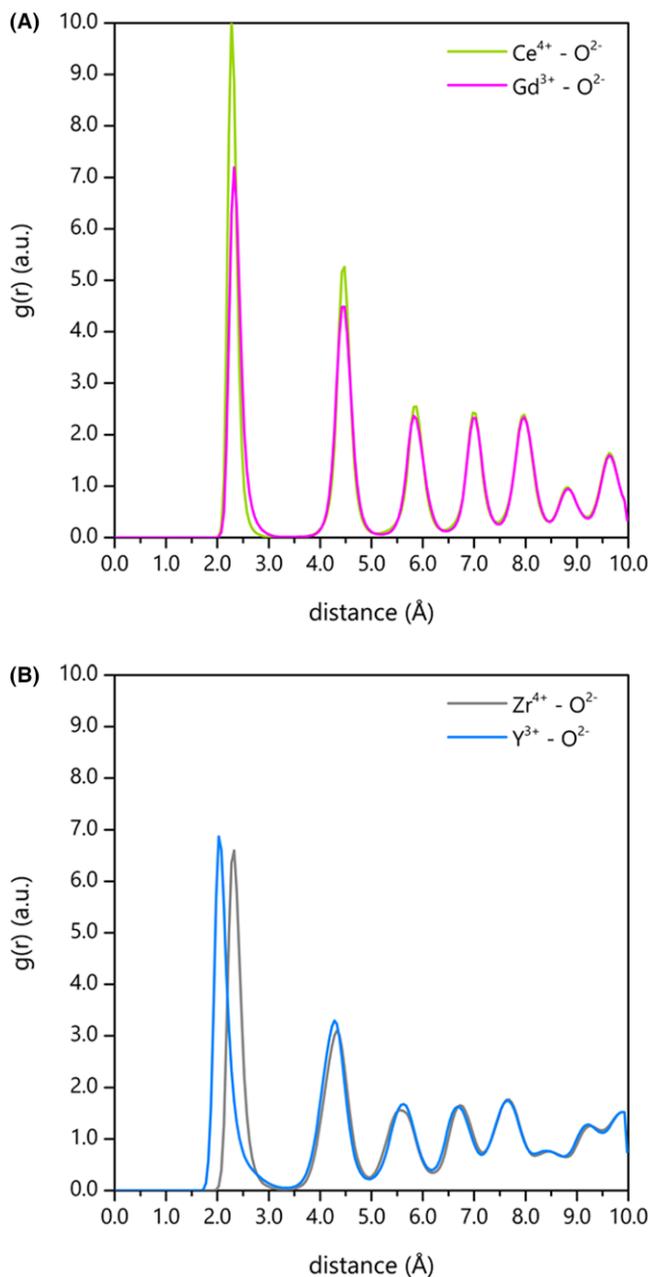

FIGURE 6 Radial distribution functions, g(r), for the different cation-anion pairs at 10 K in (A) the gadolinium-doped ceria phase and (B) the yttria-stabilized zirconia phase [Color figure can be viewed at wileyonlinelibrary.com]

RDF provides information about the average interatomic distances. So far, since we do not have experimental distances for the doped materials, we are going to use the pure bulk ones. The experimental Ce-O distance is around 2.34 Å (based on the 5.411 Å experimental lattice parameter), but the RDF indicates that the average Ce-O distance in our system is 2.28 Å, suggesting that the GDC phase could be under compression. This finding is consistent with the presence of screw dislocations and the slight bending of the GDC phase, as already discussed. Interestingly, according to the RDF, the Gd-O distances are 2.31 Å. The Gd-O distance in the experimental Gd_2O_3 unit cell oscillates between 2.29 Å and 2.32 Å, which fit perfectly the RDF of our mixed system. These values, however, do not indicate that the strain is actually influencing the Gd-O distances, but suggest that vacancies and dopants are associated. The presence of an oxygen vacancy next to the gadolinium allows it to be better accommodated in the strained matrix and consequently, Gd-O distances are more similar to the experimental ones. Conversely, this effect could not be seen for Ce-O, because the proportion of Ce atoms and oxygen vacancies is much smaller than for Gd/V_O. It is worth remembering that this structure is obtained at the end of A&R, when the simulation is performed at 10 K, thus the association between dopants and oxygen vacancies is expected.

Regarding the YSZ phase, the Zr^{4+}-O^{2-} distance derived from the experimental bulk parameter is 2.20 Å,[37] which is 0.17 Å larger than the one we obtained through the RDF analysis, which on average is only 2.03 Å. This discrepancy could be an effect of the major irregularities found in the YSZ, with more amorphous regions than in the GDC phase. For Y^{3+}-O^{2-}, experimental Y_2O_3 shows an average distance of 2.29 Å,[53] and our RDF is in excellent agreement with a distance of 2.30 Å.

These cation-oxygen distances, however, do not provide any indication whether the dopants are evenly distributed or not. However, the RDF peaks further out from the first neighboring sphere provide this information. The superposition of the peaks relating to the Ce^{4+}-O^{2-} and Gd^{3+}-O^{2-} pair, and the Zr^{4+}-O^{2-} and Y^{3+}-O^{2-} show that the dopants are well dispersed in their respective matrices (ceria and zirconia) and do not form Gd_2O_3 or Y_2O_3 domains.[33]

4.3 | Induced strain

Although dislocations help to accommodate lattice misfit, it is known that at the interface the system is strained trying to accommodate the different lattice parameters.[54] We have shown how the strain can affect the materials in Figure 4A, where the GDC phase is slightly bent. Thus, materials can also become compressed or expanded at the interface, which is one of the factors that potentially leads to

fractures. In order to gain further insight into this effect, we have performed A&R calculations, assuming that the entire system was either GDC or YSZ, and compared these pure systems with the GDC-YSZ interfacial system. In this way, we could evaluate the degree of compression or expansion that the materials suffered in the mixed system. From the unit cell values obtained for each material at 10 K after applying A&R, we have calculated the volume variation ($\Delta V\%$) according to Equation 5, where $V_{GDC/YSZ}$ represents the volume of the GDC/YSZ unit cell, and V_i represents the volume of either the GDC or the YSZ unit cell. Hence, positive values imply expansion and negative values compression of the interface with respect to the isolated materials.

$$\Delta V\% = \frac{V_{GDC/YSZ} - V_i}{V_{GDC/YSZ}} \times 100 \quad (5)$$

As observed in the data collected in Table 4, both lattice vectors and volume differences are different depending on the system that we are considering. GDC, when it is in contact with YSZ, suffers a volume compression of 7.91%, whereas YSZ experiences a slightly larger expansion of 8.85%. The lattice vectors behave in the same way, where we observe isotropic compression for GDC and isotropic expansion for YSZ. This compression/expansion pattern, in addition to the screw dislocations and some void regions near the grain boundaries between GDC/YSZ, could potentially have a strong impact on the oxygen conductivity of the system. It is worth mentioning that this effect is intrinsic only to the region near the boundary between GDC/YSZ, and it dissipates as soon as we move away from the interface.[41]

5 | CONCLUSION

In this paper we have used molecular dynamics simulations to investigate the interface between two well-known doped metal oxide materials used as electrolytes in SOFCs: GDC and YSZ. The degree of complexity these interfaces show experimentally requires a sophisticated model that includes all the different types of defects in order to obtain realistic results. To do so, we have used the A&R strategy,[20] using an initial interface that minimizes the lattice misfit between materials according to the near coincidence site lattice protocol.

The resulting mixed material had lost its initial structure and undergone a strong layer reorganization during the crystallization step. As a consequence, the lattice misfit was accommodated via dislocations that were spread through both GDC and YSZ, reflecting a more realistic system than the initial perfect crystal. A&R also allowed the diffusion of cations inside the contiguous phases, which is another aspect that has been observed experimentally. This diffusion is controlled by the randomization step during A&R and, in this particular case, it was minimized in order to avoid the formation of secondary phases or interdiffusion layers. Indeed, radial distribution functions of the cation-oxygen pairs demonstrated that no dopant clustering was formed during A&R. The small thickness of both layers, however, introduces strain effects derived from the lattice misfit between the materials. This strain provoked the compression of GDC and the expansion of YSZ, which could affect the oxygen conductivity. Oxygen ion diffusion as well as the polarization of the different ionic species will be investigated in future work.

6 | ASSOCIATED CONTENT

The electronic supporting information contains a short description of the theoretical background used in the METADISE program in order to obtain surfaces and grain boundaries, as well as a figure describing tilt and twisted grain boundaries.

AUTHOR CONTRIBUTIONS

The manuscript was written through contributions of all authors. All authors have given approval to the final version of the manuscript.

TABLE 4 Unit cell vector modules (a, b, and c) in Å, unit cell volume (V) in Å^3 for the systems GDC/YSZ, GDC, and YSZ at 10 K. $\Delta V\%$ (nondimensional) is also listed considering both GDC and YSZ as references ($\Delta V\%$ GDC and $\Delta V\%$ YSZ, respectively)

	GDC/YSZ	GDC	YSZ	$\Delta V\%$ GDC	$\Delta V\%$ YSZ
a	64.64	66.30	62.67	−2.57	3.04
b	88.88	91.16	86.17	−2.57	3.04
c	153.52	157.46	148.85	−2.57	3.04
V	8.82×10^5	9.52×10^5	8.04×10^5	−7.91	8.85

REFERENCES

1. Mahato N, Banerjee A, Gupta A, Omar S, Balani K. Progress in material selection for solid oxide fuel cell technology: a review. *Prog Mater Sci*. 2015;72:141-337.

2. Cowin PI, Petit CTG, Lan R, Irvine JTS, Tao S. Recent progress in the development of anode materials for solid oxide fuel cells. *Adv Energy Mater*. 2011;1:314-332.

3. Sun C, Li H, Chen L. Nanostructured ceria-based materials: synthesis, properties, and applications. *Energy Environ Sci*. 2012;5:8475-8505.

4. Kim SJ, Kim KJ, Choi GM. Effect of $Ce_{0.43}Zr_{0.43}Gd_{0.1}Y_{0.04}O_{2-\delta}$ contact layer on stability of interface between GDC interlayer and YSZ electrolyte in solid oxide electrolysis cell. *J Power Sources*. 2015;284:617-622.

5. Piroonlerkgul P, Wiyaratn W, Soottitantawat A, et al. Operation viability and performance of solid oxide fuel cell fuelled by different feeds. *Chem Eng J*. 2009;155:411-418.

6. Ni M, Leung MKH, Leung DYC. Technological development of hydrogen production by solid oxide electrolyzer cell (SOEC). *Int J Hydrogen Energy*. 2008;33:2337-2354.

7. Zhang C, Li C-J, Zhang G, et al. Ionic conductivity and its temperature dependence of atmospheric plasma-sprayed yttria stabilized zirconia electrolyte. *Mater Sci Eng, B*. 2007;137:24-30.

8. Politova TI, Irvine JTS. Investigation of scandia–yttria–zirconia system as an electrolyte material for intermediate temperature fuel cells—influence of yttria content in system $(Y_2O_3)_x(Sc_2O_3)_{(11-x)}(ZrO_2)_{89}$. *Solid State Ionics*. 2004;168:153-165.

9. Inaba H, Tagawa H. Ceria-based solid electrolytes. *Solid State Ionics*. 1996;83:1-16.

10. Kindermann L, Das D, Nickel H, Hilpert K. Chemical compatibility of the $LaFeO_3$ base perovskites $(La_{0.6}Sr_{0.4})_zFe_{0.8}M_{0.2}O_3 - \delta$ (z = 1, 0.9; M = Cr, Mn Co, Ni) with yttria stabilized zirconia. *Solid State Ionics*. 1996;89:215-220.

11. Matsui T, Komoto M, Muroyama H, Kishida K, Inui H, Eguchi K. Degradation factors in $(La, Sr)(Co, Fe)O_{3-\delta}$ cathode/$Sm_2O_3–CeO_2$ interlayer/$Y_2O_3–ZrO_2$ electrolyte system during operation of solid oxide fuel cells. *J Power Sources*. 2016;312:80-85.

12. Wilde V, Störmer H, Szász J, Wankmüller F, Ivers-Tiffée E, Gerthsen D. Effect of $Gd_{0.2}Ce_{0.8}O_2$ sintering temperature on formation of a $SrZrO_3$ blocking layer between $Y_{0.16}Zr_{0.84}O_2$, $Gd_{0.2}Ce_{0.8}O_2$ and $La_{0.58}Sr_{0.4}Co_{0.2}Fe_{0.8}O_3$. *ECS Trans*. 2015;66:103-107.

13. Szász J, Wankmüller F, Wilde V, et al. Nature and functionality of oxygen/cathode/electrolyte-interfaces in SOFCs. *ECS Trans*. 2015;66:79-87.

14. Uchida H, Arisaka SI, Watanabe M. High performance electrode for medium-temperature solid oxide fuel cells $La(Sr)CoO_3$ cathode with ceria interlayer on zirconia electrolyte. *Electrochem Solid-State Lett* 1999;2:428-430.

15. Timurkutluk B, Timurkutluk C, Mat MD, Kaplan Y. Novel structured gadolinium doped ceria based electrolytes for intermediate temperature solid oxide fuel cells. *J Power Sources*. 2011;196:9361-9364.

16. Teocoli F, Ni DW, Brodersen K, Foghmoes SPV, Ramousse S, Esposito V. Effects of co-sintering in self-standing CGO/YSZ and CGO/ScYSZ dense bi-layers. *J Mater Sci*. 2014;49:5324-5333.

17. Zhou XD, Scarfino B, Anderson HU. Electrical conductivity and stability of Gd-doped ceria/Y-doped zirconia ceramics and thin films. *Solid State Ionics*. 2004;175:19-22.

18. Kah Chun L., Brett ID. Molecular dynamics simulation of yttria-stabilized zirconia (YSZ) crystalline and amorphous solids. *J Phys: Condens Matter* 2011;23:035401.

19. Martin P, Parker SC, Sayle DC, Watson GW. Atomistic modeling of multilayered ceria nanotubes. *Nano Lett*. 2007;7:543-546.

20. Sayle DC. The predicted 3-D atomistic structure of an interfacial screw-edge dislocation. *J Mater Chem*. 1999;9:2961-2964.

21. Watson GW, Kelsey ET, de Leeuw NH, Harris DJ, Parker SC. Atomistic simulation of dislocations, surfaces and interfaces in MgO. *J Chem Soc, Faraday Trans*. 1996;92:433-438.

22. Tasker PW. Surface energies, surface tensions and surface-structure of the alkali-halide crystals. *Philos Mag A*. 1979;39:119-136.

23. Todorov IT, Smith W, Trachenko K, Dove MT. DL_POLY_3: new dimensions in molecular dynamics simulations via massive parallelism. *J Mater Chem*. 2006;16:1911-1918.

24. Todorov IT, Smith W.. DL_POLY_3: the CCP5 national UK code for molecular–dynamics simulations. *Philos Trans R Soc London, A* 2004;362:1835-1852.

25. Smith W, Forester TR. DL_POLY_2.0: a general-purpose parallel molecular dynamics simulation package. *J Mol Graphics Modell*. 1996;14:136-141.

26. Dwivedi A, Cormack AN. A computer simulation study of the defect structure of calcia-stabilized zirconia. *Philos Mag A*. 1990;61:1-22.

27. Sayle TXT, Parker SC, Catlow CRA. The role of oxygen vacancies on ceria surfaces in the oxidation of carbon monoxide. *Surf Sci*. 1994;316:329-336.

28. Lewis GV, Catlow CRA. Potential models for ionic oxides. *J Phys C* 1985;18:1149.

29. Balducci G, Kašpar J, Fornasiero P, Graziani M, Islam MS. Surface and reduction energetics of the $CeO_2−ZrO_2$ catalysts. *J Phys Chem B*. 1998;102:557-561.

30. Sayle TXT, Parker SC, Catlow CRA. Surface oxygen vacancy formation on CeO_2 and its role in the oxidation of carbon monoxide. *J Chem Soc, Chem Commun* 1992;977-978. doi: 10.1039/C39920000977

31. Sayle DC, Maicaneanu SA, Watson GW. Atomistic models for $CeO_2(111)$, (110), and (100) nanoparticles, supported on yttrium-stabilized zirconia. *J Am Chem Soc*. 2002;124:11429-11439.

32. Balducci G, Islam MS, Kašpar J, Fornasiero P, Graziani M. Reduction process in $CeO_2−MO$ and $CeO_2−M_2O_3$ mixed oxides: a computer simulation study. *Chem Mater*. 2003;15:3781-3785.

33. Sayle TXT, Parker SC, Sayle DC. Ionic conductivity in nano-scale CeO_2/YSZ heterolayers. *J Mater Chem*. 2006;16:1067-1081.

34. Essmann U, Perera L, Berkowitz ML, Darden T, Lee H, Pedersen LG. A smooth particle mesh Ewald method. *J Chem Phys*. 1995;103:8577-8593.

35. Hoover WG. Canonical dynamics: equilibrium phase-space distributions. *Phys Rev A*. 1985;31:1695-1697.

36. Gerward L, Staun Olsen J, Petit L, Vaitheeswaran G, Kanchana V, Svane A. Bulk modulus of CeO_2 and PrO_2—An experimental and theoretical study. *J Alloys Compd* 2005;400:56-61.

37. Aldebert P, Traverse J-P. Structure and ionic mobility of zirconia at high temperature. *J Am Ceram Soc*. 1985;68:34-40.

38. Cadi-Essadek A, Roldan A, de Leeuw NH. Ni deposition on yttria-stabilized $ZrO_2(111)$ surfaces: a density functional theory study. *J Phys Chem C*. 2015;119:6581-6591.

39. Li X, Feng Z, Lu J, Wang F, Xue M, Shao G. Synthesis and electrical properties of $Ce_{1−x}Gd_xO_{2−x/2}$ (x = 0.05–0.3) solid

solutions prepared by a citrate–nitrate combustion method. *Ceram Int*. 2012;38:3203-3207.

40. Martínez-Amesti A, Larrañaga A, Rodríguez-Martínez LM, et al. Chemical compatibility between YSZ and SDC sintered at different atmospheres for SOFC applications. *J Power Sources*. 2009;192:151-157.

41. Chen CH, Kiguchi T, Saiki A, Wakiya N, Shinozaki K, Mizutani N. Characterization of defect type and dislocation density in double oxide heteroepitaxial CeO_2/YSZ/Si(001) films. *Appl Phys A*. 2003;76:969-973.

42. Kiguchi T, Konno TJ, Wakiya N, Morioka H, Saito K, Shinozaki K. Nanostructure and strain analysis of CeO_2/YSZ strained superlattice. *Mater Sci Eng, B*. 2010;173:220-228.

43. Harris DJ, Farrow TS, Harding JH, et al. Surface diffusion and surface growth in nanofilms of mixed rocksalt oxides. *Phys Chem Chem Phys*. 2005;7:1839-1844.

44. Fisher CAJ, Matsubara H. Molecular dynamics simulations of interfaces between NiO and cubic ZrO_2. *Philos Mag*. 2005;85:1067-1088.

45. Sayle TXT, Catlow CRA, Sayle DC, Parker SC, Harding JH. Computer simulation of thin film heteroepitaxial ceramic interfaces using a near-coincidence-site lattice theory. *Philos Mag A*. 1993;68:565-573.

46. Bogicevic A, Wolverton C, Crosbie GM, Stechel EB. Defect ordering in aliovalently doped cubic zirconia from first principles. *Phys Rev B* 2001;64:014106.

47. Lee HB, Prinz FB, Cai W. Atomistic simulations of surface segregation of defects in solid oxide electrolytes. *Acta Mater*. 2010;58:2197-2206.

48. Gao Z, Kennouche D, Barnett SA. Reduced-temperature firing of solid oxide fuel cells with zirconia/ceria bi-layer electrolytes. *J Power Sources*. 2014;260:259-263.

49. Kazlauskas S, Kežionis A, Šalkus T, Orliukas A. Effect of sintering temperature on electrical properties of gadolinium-doped ceria ceramics. *J Mater Sci*. 2015;50:3246-3251.

50. Knibbe R, Hjelm J, Menon M, et al. Cathode–electrolyte interfaces with CGO barrier layers in SOFC. *J Am Ceram Soc*. 2010;93:2877-2883.

51. Liang B, Tao T, Zhang S, Huang Y, Cai Z, Lu S. Asymmetric diffusion of Zr, Sc and Ce, Gd at the interface between zirconia electrolyte and ceria interlayer for solid oxide fuel cells. *J Alloys Compd*. 2016;679:191-195.

52. Yashima M. Invited Review: some recent developments in the atomic-scale characterization of structural and transport properties of ceria-based catalysts and ionic conductors. *Catal Today*. 2015;253:3-19.

53. Ferreira FF, Granado E, Carvalho W Jr, Kycia SW, Bruno D, Droppa R Jr. X-ray powder diffraction beamline at D10B of LNLS: application to the Ba_2FeReO_6 double perovskite. *J Synchrotron Rad*. 2006;13:46-53.

54. Hjalmarsson P, Sun X, Liu Y-L, Chen M. Influence of the oxygen electrode and inter-diffusion barrier on the degradation of solid oxide electrolysis cells. *J Power Sources*. 2013;223:349-357.

SUPPORTING INFORMATION

Additional Supporting Information may be found online in the supporting information tab for this article.